Crustal deformation in Taiwan: Results from finite source inversions of six M_w > 5.8 Chi-Chi aftershocks

Wu-Cheng Chi[1] and Doug Dreger

Seismological Laboratory, University of California, Berkeley, California, USA

[1] We inverted strong motion data for the finite source parameters of six large aftershocks of the 1999 Chi-Chi, Taiwan, earthquake to investigate seismogenic structure in Taiwan. For each event we derived a preferred model by testing different focal mechanisms, hypocenters, rupture velocities, and dislocation risetimes, as well as different combinations of stations in more than 1000 inversions. We documented how the fits between the waveforms and the corresponding synthetics deteriorated as the hypocenter and focal mechanism deviate from those of the preferred model. If the deviation in focal mechanisms and hypocenters is less than 20° and 5 km, respectively, we generally recovered 80% of the preferred model's synthetic waveform fit. Unlike the dislocation risetime, the rupture velocity used in the inversion had a strong influence on the waveform fits in this study. We also used the slip models to study fault geometry. Two of the aftershocks ruptured on the southern extension of the main shock slip area. One strike-slip aftershock nucleated within the basement but ruptured mainly within the overlying sedimentary strata, suggesting that seismogenic deformation in the basement can influence shallow structures. P axes of the derived models have azimuths consistent with current plate motion. Finally, GPS displacement derived from the six slip models can explain 80% of the postseismic deformation observed in the aftershock regions, indicating that studies of postseismic deformation must take into account the cumulative effects of large, shallow aftershocks.   *INDEX TERMS:* 7215 Seismology: Earthquake parameters; 7230 Seismology: Seismicity and seismotectonics; 7223 Seismology: Seismic hazard assessment and prediction; 7294 Seismology: Instruments and techniques; 8105 Tectonophysics: Continental margins and sedimentary basins (1212); *KEYWORDS:* Taiwan, earthquake, finite source processes, basement deformation, strong motion, seismic hazard mitigation

1. Introduction

[2] More than 30,000 aftershocks occurred in the 3 months following the Chi-Chi, Taiwan, earthquake (M_w = 7.6). Among them, more than six aftershocks with M_w > 5.8 were well recorded by a strong motion network maintained by the Central Weather Bureau of Taiwan. They provided an unprecedented opportunity to study the finite source process of moderate sized earthquakes (1) to characterize the ground motion in Taiwan, especially in urban area, (2) to derive source parameters of the moderate to large aftershocks, (3) to study the robustness and sensitivities of the inversion results by testing wide ranges of input parameters in the inversions, and (4) to study the active fault system in the region, especially in the seismogenic midcrust level.

[3] Here we document finite source inversions and sensitivity tests for six of the aftershocks (Table 1) for which strong motion data are available. Each aftershock was recorded by more than 200 strong motion stations. We use only data from stations that had no apparent timing errors and provide good azimuthal coverage (Figures 1a and 1b). Using a preliminary slip model, for each event we tested a range of values for each of the source parameters: the slip vector, fault orientation, location, hypocentral depth, rupture velocity, and dislocation risetime. In this modeling, we assumed that the rupture velocity and dislocation risetime were constant and did not vary spatially. For each event we performed more than 1000 sensitivity tests by varying the source parameters used in the inversions, and we then documented the influence that these parameters have on the slip model and on the waveform fits (Table 2). To determine what the contributions of individual stations are and whether the results might be biased, we applied "jackknife tests." That is, we examined the fits of the waveforms from the inversions for which we excluded the data from one station at a time until we have tested all the stations in the preferred model.

---

[1]Now at Seismological Laboratory, California Institute of Technology, Pasadena, California, USA.

Table 1. Source Parameters and Results of the Inversions[a]

	Event					
	1	2	3	4	5	6
Origin date	20 Sept.	20 Sept.	20 Sept.	22 Sept.	25 Sept.	22 Oct.
Origin time, UT	1757:15.310	1803:41.160	2146:37.490	0014:40.770	2352:49.509	0218:56.930
Longitude	121.01 ± 0.03	120.86 ± 0.03	120.82 ± 0.04	121.08 ± 0.04	121.01 ± 0.03	120.45 ± 0.03
Latitude	23.94 ± 0.02	23.81 ± 0.05	23.60 ± 0.04	23.81 ± 0.06	23.87 ± 0.04	23.53 ± 0.04
Depth, km	8 ± 5	8 ± 4	18 ± 8	10 ± 8	16 ± 7	16 ± 6
M_0, dyn cm	7.15e + 024[b]	2.53e + 25	2.2e + 25	2.5e + 25	3.7e + 25	1.7e + 25
M_w	5.8	6.2	6.2	6.2	6.3	6.1
Strike, deg	200 ± 25	0 ± 20	330 ± 15	165 ± 25	5 ± 15	20 ± 30
Dip, deg	41 ± 25	10 ± 20	89 ± 10	70 ± 25	30 ± 10	75 ± 10
Rake, deg	78 ± 25	80 ± 20	15 ± 15	100 ± 25	100 ± 10	90 ± 15
S/D/R, M_w[c]						
Harvard CMT	N/A	N/A	336/89/1, 6.4	183/80/97, 6.4	12/20/95, 6.5	46/52/125, 5.8
NEIC	N/A	N/A	N/A	187/69/108, 6.3	N/A	26/55/103, 5.9
ERI	N/A	N/A	N/A	175/85/88, 6.4	35/25/115, 6.4	5/44/74, 5.9
BATS	N/A	329/35/59, 6.2	242/55/−157, 6.3	13/25/124, 6.2	50/44/126, 6.2	219/29/129, 5.9
CHEN (M_L)	N/A	N/A	N/A	161/69/87, 6.8	351/25/60, 6.8	N/A
V_{rup}, km/s	1.5 (1.3–2.6)	1.6 (1.3–3.5)	2.4 (2.0–2.8)	2.6 (2.0–3.0)	3.2 (1.8–3.6)	2.0 (1.6–2.3)
DRT, s	0.2 (0.1–0.6)	0.2 (0.1–0.8)	0.7 (0.2–0.9)	0.7 (0.1–0.9)	0.3 (0.1–0.9)	0.3(0.1–0.9)
Maximum slip, cm	46	231	85	83	162	205
Stress drop, MPa	5.3	6.2	3.8	4.6	5.9	9.9
Asperity dimension, km × km	12 × 4	10 × 10	5 × 25	6 × 20	6 × 22	4 × 14
Fault dimension, km × km	24 × 24	14 × 15	24 × 19	24 × 36	30 × 21	18 × 18
Number of stations	13	13	9	9	11	14
VR, %	46	56	56	48	72	60
Confidence level	low	high	high	Low	high	Low
CF S/D/R, VR, %	35/50/100, 48	190/80/92, 43	240/75/179, 42	318/22/64, 23	173/61/84, 55	200/15/90, 46

[a]S/D/R, strike/dip/rake; VR, variance reduction; CF, conjugate fault; V_{rup}, rupture velocity; DRT, dislocation risetime; values in parentheses indicate range of values tested; N/A, not available.

[b]Read 7.15e + 024 as 7.15×10^{24}.

[c]CMT, centroid moment tensor; NEIC, National Earthquake Information Center; ERI, Earthquake Research Institute, University of Tokyo, Web site; BATS, Broadband Array in Taiwan for Seismology; CHEN, *Chen et al.* [2002].

With these tests we were able to derive a preferred slip model that was stable and gave good waveform fits, and which has the uncertainties documented. Previously, the rupture fault planes of the aftershocks were unknown, as none of these aftershocks ruptured the surface, nor had rupture planes unambiguously defined by smaller aftershock seismicity. These inversions were also used to determine the orientation of the causative plane and to provide an estimate of the confidence in the chosen plane.

[4] The Chi-Chi sequence also provides a great opportunity for using earthquake sources to map the deep crustal structures of Taiwan. Several seismicity and moment tensor studies have already illuminated the geometry of important seismogenic faults at depth [e.g., *Kao and Chen*, 2000; *Hirata et al.*, 2000; *Carena et al.*, 2002; *Chen et al.*, 2002]. To make the tectonic interpretation easier, we want to connect these data "points" in three dimensions using the planes of the planar slip models derived from the results of our finite fault inversion.

[5] All of these results are important for seismic hazard mitigation. The causative faults derived from this study, all of which are blind, can be added to the map of active faults in Taiwan. The slip models of the main shock and aftershocks can be used to study (1) stress perturbation, (2) earthquake source scaling relationships, and (3) attenuation relationships for engineering purposes. Also, the extensive sensitivity tests document how variations in the input source parameters affect the waveform fits derived from the finite fault inversions. As a result, these studies provide the information needed to evaluate the performance of the seismic network if we want to invert the finite fault

parameters in real time and use the source model to forward model the ShakeMaps.

2. Regional Tectonic Setting of Taiwan

[6] Central Taiwan is located in the collision zone between the Luzon arc of the Philippine Sea plate and the Chinese passive margin of the Eurasia plate. The relative plate motion is ∼80 mm/yr in the N66°W direction [*Yu et al.*, 2001]. Here the Chinese continental passive margin, with normal and strike-slip fault structures, enters into the convergent boundary where contractional processes dominate. *Suppe* [1981] has proposed that most of the sediments above the basement are being incorporated into the Taiwan fold and thrust belt by westward propagation of a low-angle east dipping decollement fault beneath the mountain belt. However, the shortening style below the decollement is less understood. The basement may act as a relatively rigid body underthrusting the mountain belt [*Suppe*, 1981, 1984], or it may deform internally to thicken the crust in Taiwan [*Rau and Wu*, 1995].

3. Chi-Chi, Taiwan, Earthquake and Its Aftershocks

[7] Seismicity and moment tensor studies of the Chi-Chi earthquake sequence have already provided important constraints on the crustal geometry. *Kao and Chen* [2000] proposed that the aftershocks occurred on two parallel, low-angle east dipping faults, one in the vicinity of the proposed decollement and a second 15 km below it (Figure 1a, inset).
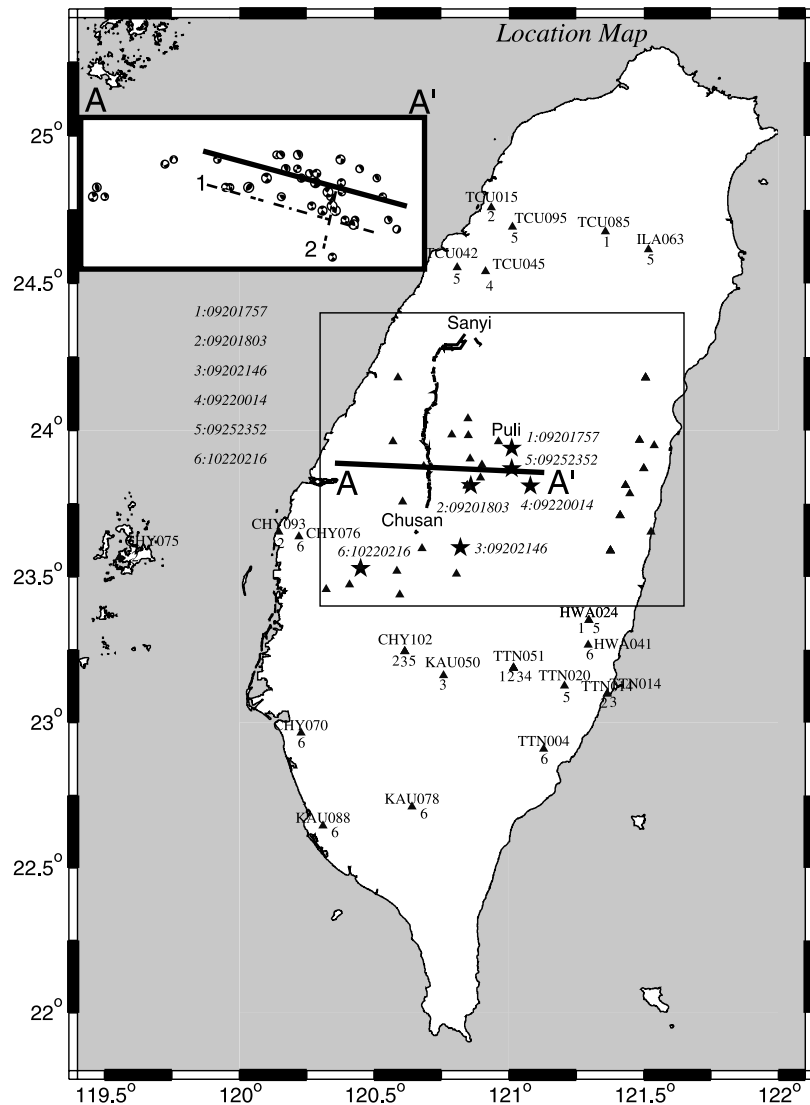
Figure 1a. Location map. Stars show the locations of the six aftershocks. Triangles are the strong motion stations. The numbers below each triangle are the event/events for which this station was used. Surface rupture from the main shock is plotted for reference. The main shock asperity is bounded by the towns Sanyi, Puli, and Chusan [*Chi et al.*, 2001]. The inset cross section shows a schematic with moment tensor solutions for some events of the Chi-Chi earthquake sequence [*Kao and Chen*, 2000] near these six large aftershocks. Two models have been proposed to explain these moment tensor results. Both have an east dipping decollement represented by the solid line. One model (model 1) proposes another east dipping fault under the decollement [*Kao and Chen*, 2000], while another model (model 2) suggests that some of the seismicity below the decollement is on a west dipping fault [*Carena et al.*, 2002; *Chen et al.*, 2002].

The upper decollement is also illuminated in an aftershock study by *Hirata et al.* [2000], although with a shallower dip. *Carena et al.* [2002] suggested a low-angle east dipping detachment under most of central and eastern Taiwan, with a separate seismicity zone beneath the detachment dipping to the west. *Chen et al.* [2002] also presented evidence for this west dipping seismic zone on the basis of their relocations of events and the focal mechanisms that they determined (compare the basement-involved west dipping fault in Figure 1a). Overall, the aftershocks are well located. However, the uncertainties in focal depths and the ambiguity in determining the causative fault planes from moment tensor or first-motion solutions have prompted different interpretations of the fault geometry. In addition, some of the large aftershocks in the vicinity of the decollement consistently have one nodal plane dipping 30°–40° to the east [e.g., *Kao and Chen*, 2000], steeper than the proposed shallowly dipping decollement. As a result, these aftershocks could have ruptured either on the shallowly east dipping decollement, on the west dipping back thrusts above the decollement, on the steeper east dipping splay faults above the decollement, or even on steep west dipping basement-involved reverse faults under the decollement (Figure 1b, inset).
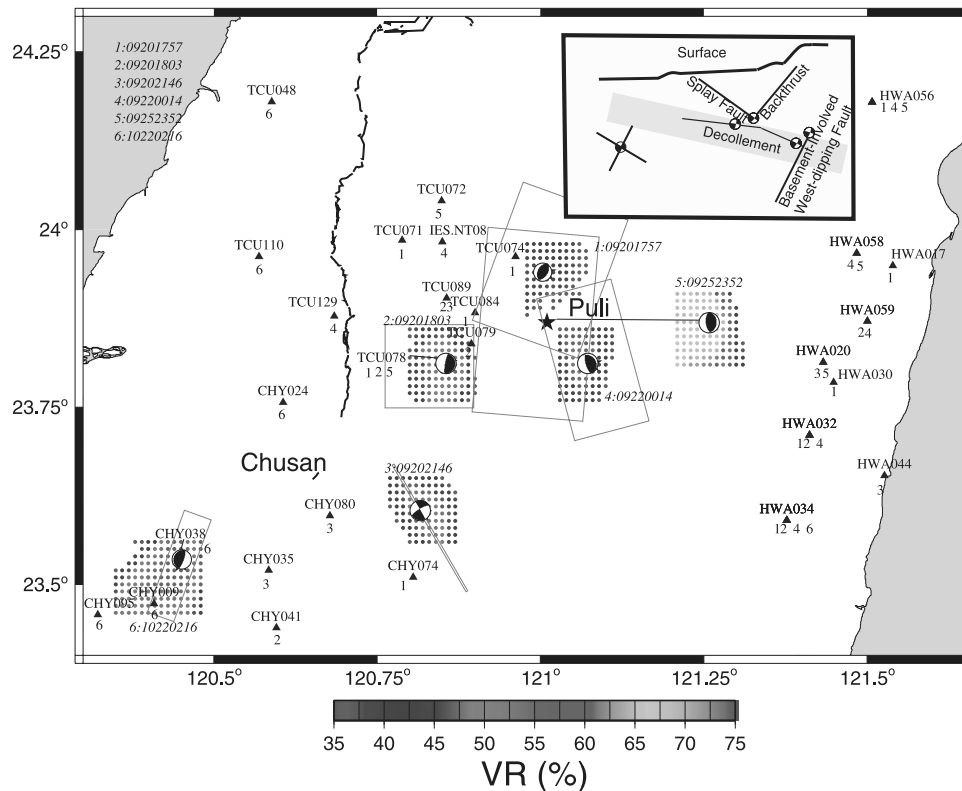
Figure 1b. Enlargement of box on Figure 1a. The focal mechanisms are plotted at the preferred epicenters. The dot color shows the variance reduction derived from inversions using that particular location as epicenter. It shows how rapidly the waveform fits, measured by variance reduction (VR), deteriorate if the epicentral information is incorrect. Results for event 5 are shifted to the east for clear presentation. The blue rectangles are the fault dimensions of the preferred slip models. Note that events 2 and 5 are located along the lineation defined by the towns Puli and Chusan. *Chi et al.* [2001] have proposed that main shock rupture stopped along this lineation. The inset cross section shows a schematic with possible rupture scenarios for the aftershocks that we studied. Depending on the causative fault plane and its dip angle, these aftershocks might have ruptured on the decollement, an east dipping splay fault, a back thrust, or a basement-involved fault. See color version of this figure at back of this issue.

[8] The finite source process of the main shock has been studied extensively using various combinations of strong motion, teleseismic, and GPS data [e.g., *Yagi and Kikuchi*, 2000; *Kikuchi et al.*, 2000; *Ma et al.*, 2000, 2001; *Zeng and Chen*, 2001; *Mori and Ma*, 2000; *Ji et al.*, 2001; *Wu et al.*, 2001; *Chi et al.*, 2001; *Loevenbruck et al.*, 2001; *Johnson et al.*, 2001]. To a first order, the source models are all consistent, showing large slip to the north of the focus at shallow depths. Slip to the south tends to be less constrained. There is evidence that the extent of main shock rupture may have been structurally controlled, and *Chi et al.* [2001] suggest that the main shock asperity terminated in the south along a seismic lineation between the towns of Puli and Chusan (Figures 1a and 1b).

[9] Excellent GPS displacement data have been collected for the preevent, coseismic, and postseismic epochs [*Yu et al.*, 2001]. More than 10 m of horizontal coseismic displacement was found in the northern region of the surface rupture. There are also >10 cm of displacement recorded 3 months after the main shock, mostly in the southern section of the surface rupture [*Hsu et al.*, 2002], where the large aftershocks occurred.

[10] Through finite fault inversions we determined the causative fault planes and the slip models of these six aftershocks. We compare our results with published seismicity data to make a tectonic interpretation to understand if there is basement-involved coseismic deformation and if some of the thrusts ruptured on a west dipping fault.

4. Strong Motion Data and Method

[11] In this study we use seismic waveforms from the strong motion network of the Central Weather Bureau (CWB) of Taiwan, which has an average station spacing of 5 km, except in the central highlands [*Lee et al.*, 2001]. We also include data from the Institute of Earth Sciences (IES), Academia Sinica of Taiwan, for some of the events. Overall, more than 200 accelerometers with sample rates of either 200 or 250 samples per second, recorded each of the six large aftershocks. We have converted each waveform from digital counts to cm/s^2, removed the mean offset, integrated from acceleration to velocity, and band-pass filtered between 0.02 and 0.5 Hz with a four-pole acausal Butterworth filter before resampling the data to 10 samples per second.

[12] Using a frequency–wave number code from *Saikia* [1994], we calculated a catalog of Green's functions for an average one-dimensional (1-D) velocity model (Table 3) taken from a 3-D tomographic study by *Rau and Wu* [1995]. This 1-D model had been tested in routine regional moment tensor studies of local and regional events [cf. *Kao and Chen*, 2000] and performed well in the finite fault inversions of Chi-Chi main shock [*Chi et al.*, 2001] and an aftershock [*Chi and Dreger*, 2002]. The Green's functions were subjected to the same signal processing. In this frequency range (0.02–0.5 Hz) the 1-D Green's function might not totally represent the wave field from the complex 3-D velocity structures of Taiwan. However, we found that we can model the low-frequency part of the waveform relatively well, especially the first direct wave part of the waveforms.

[13] We used strong motion data to invert the representation theorem (equation (1)) [*Aki and Richards*, 1980] using a method pioneered by *Hartzell and Heaton* [1983]. The observed seismograms are used to calculate the spatiotemporal slip distribution, $u_i(\xi, \tau)$, over a plane where

$$u_n(x,t) = \int_{-\infty}^{\infty} d\tau \iint_{\Sigma} [u_i(\xi,\tau)]c_{ijpq}v_j\partial G_{np}(x,t-\tau;\xi,0)/\partial\xi_q d\Sigma,$$

(1)

where

u_n nth component of observed velocity;
c_{ijpq} fourth-order elasticity tensor;
v_j fault orientation unit vector;
G_{np} Green's function;
x vector describing the relative location of the source and receiver;
ξ, τ spatial and temporal variables of integration.

[14] In equation (1), n refers to the ground motion component and i, j, p, and q are orientation indices. The quantity $u_i(\xi, \tau)c_{ijpq}v_j$ is equivalent to $m(\xi, \tau)$, the seismic moment tensor which changes in space and time. The quantity $u_i(\xi, \tau)$ is the spatiotemporal slip information to be determined by inverting the data.

[15] We use a damped, linear least squares inversion to determine the spatiotemporally discretized slip. For each grid point (subfault) on the gridded fault plane we calculate

Table 2. Parameters Tested in the Inversions[a]

| | Event | | | | | |
	1	2	3	4	5	6
Origin time	0920/17:57:15.310	0920/18:03:41.160	0920/21:46:37.490	0922/00:14:40.770	0925/23:52:49.509	1022/02:18:56.930
Longitude	121.00–121.06, 0.01	120.80–120.91, 0.01	120.77–120.87, 0.01	121.03–121.13, 0.01	120.96–121.06, 0.01	120.35–120.45, 0.01
Latitude	23.90–23.96, 0.01	23.76–23.86, 0.01	23.56–23.65, 0.01	23.76–23.86, 0.01	23.81–23.91, 0.01	23.46–23.56, 0.01
Depth, km	2–30, 2	2–30, 2	2–24, 2	6–34, 2	2–30, 2	6–26, 2
V_{rup}, km/s	0–3.2, 0.1	1.0–3.2, 0.2	1.0–2.8, 0.1	1.0–3.6, 0.2	0.2–3.6, 0.2	1.0–4.0, 0.1
DRT, s	0.1–1.0, 0.1	0.1–1.0, 0.1	0.2–1.0, 0.1	0.1–1.0, 0.1	0.1–0.9, 0.1	0.1–0.9, 0.1
Strike,[b] east dipping	320 330 340 350 0 10 20 25 30 35 40 50 60	355 0 5 10 15 20 25 30 35 40	310 320 325 330 335 340 350 0	330 340 350 0 10 20	0 5 10 15 20 15 30 35 40	0 10 20 30 40 50 60
Dip,[b] east dipping	10 20 30 40 50 60 70 80	5 10 15 20 25 30 35	80 85 89	10 20 30 40 50 60	10 15 20 25 30 40 45 50 55	50 55 60 65 70 75 80 85
Rake,[b] east dipping	60 70 80 90 100 110 120 130	70 80 85 90 100 110 120	–5 0 5 10 15 20 25 30	70 80 90 100 110 120	085 090 095 100 105 110 115 120 125	60 70 80 90 95 100 110 120 130
Strike,[b] west dipping	150 160 170 180 190 200 210	170 180 190 200 210	185 190 200 210 220 230 240 250	140 145 150 155 160 165 170 190 195 200 205 210 215	160 170 180 190 200 210 220 230	170 180 190 200 210 220
Dip,[b] west dipping	20 30 40 50 60 70 80	45 55 65 75 85	60 70 80 85	40 50 60 65 70 75 80 85	30 40 50 60 70 80	5 10 15 20 25 30 35 40 50
Rake,[b] west dipping	40 50 60 70 80 90 100	70 80 90 100 110 120	140 150 160 170 180	70 80 90 100 110 120	50 60 70 80 90 100	50 60 70 80 90 100 110 120

[a]For latitude, longitude, depth, rupture velocity (V_{rup}), dislocation risetime (DRT), the formats are minimum–maximum, increment.
[b]Values tested for this study.

Table 3. One-Dimensional Velocity Model Used for Green's Function Calculation[a]

Thickness, km	Depth, km	V_p, km/s	V_s, km/s	Density, g/cm^3	Q_p	Q_s
2.2	2.2	4.5	2.6	1.8	200	100
2.2	4.4	4.85	2.8	2.05	600	300
2.2	6.6	5.3	3.06	2.25	600	300
2.2	8.8	5.6	3.23	2.39	600	300
4.5	13.3	5.84	3.37	2.5	600	300
4.5	17.8	6.13	3.54	2.64	600	300
7.5	25.3	6.28	3.63	2.7	600	300
8.5	33.8	6.6	3.81	2.85	600	300
5	38.3	6.87	3.97	2.97	600	300
21.5	60.3	7.43	4.29	3.3	600	300
25	85.3	7.8	4.5	3.3	600	300

[a]Q_s and Q_p are quality factors for S and P waves, respectively.

the slip amplitude using a prescribed slip vector direction. Because of the relatively small magnitude of the aftershocks compared with the main shock, we use a single time window with a fixed dislocation risetime propagating away from the hypocenter with a spatially constant rupture velocity. The absolute times of the waveforms were tested by aligning the data with the Green's functions in time. Laplacian smoothing, moment minimization constraints, and slip positivity are implemented to improve the stability of the nonnegative least squares inversion of *Lawson and Hanson* [1974].

[16] The modeled planar fault is composed of many 1 km by 1 km subfaults. We use the relatively small dimensions of the subfault to allow the rupture front to propagate from one subfault to the neighboring subfaults with a reasonable rupture velocity. Given the range of rupture velocity that fits the data (1.5–3.2 km/s), maximum propagation delays across the subfault diagonally range from 0.4 to 0.9 s. Because the data are low-pass filtered at 2-s period, this is an adequate level of discretization. However, because the dislocation risetime for these events can be <0.4 s, our ability to resolve the risetime is poor.

[17] A range of values for the following source parameters (Table 2) has been tested to examine their effects on the waveform fits. In this way we were able to identify which parameters have stronger influence on the inversions.

[18] The waveform fits for the initial inversions are usually not good, especially if some seismograms have apparent timing errors or large-amplitude phases due to crustal 3-D velocity heterogeneity, or incorrect source parameters were used as input in the inversions. To avoid timing problems, we picked stations with arrival times similar to the arrival time predicted by our 1-D velocity model, as was done by *Chi et al.* [2001]. Horizontal particle motion for each station was plotted in map view to help identify and avoid stations with abnormally large particle motion compared to neighboring stations, assuming that the complex waveforms were due to strong local site effects, which can not be modeled using a single 1-D model. In the future, the complex waveforms can be studied when a more detailed and accurate 3-D velocity model of Taiwan is available. For each aftershock we have tested all of the published moment tensor solutions, some of which have very different focal mechanisms and source depths. Using the reported moment magnitude, we parameterized the fault dimensions, and dislocation risetimes using the relationships published by *Sommerville et al.* [1999]. If necessary, we adjusted the fault dimensions for each individual aftershock. We increased the fault dimension if the slip terminated at the edge. We reduced the size of the fault if some energy from later parts of the waveforms was mapped into the slip model, typically toward the edges of the fault plane away from the slip patches close to the hypocenter. Some of the later slip might have been scattered wave fields and not related to the earthquake source. To examine whether the "later slip" is due to source or scattering, we can use only the later slip to forward model the wave field to see which stations and seismic phases contribute to these aspects of the model in a manner similar to that of *Chi et al.* [2001].

[19] Once we had an initial model with an optimal configuration of stations, we did a grid search over a range of source parameters, including the direction of the slip vector, the fault orientation, the hypocentral location, the rupture velocity, and the dislocation risetime (Table 2). We varied these source parameters one at a time, running the inversion using the new input parameter, and then studied the changes in slip model and waveform fits. Thus we were able to document the sensitivity of the synthetics and their fits to the waveforms to each of these source parameters and to estimate the uncertainty in each of the preferred source parameters. For this purpose we define the error bounds as 10% of the variance reduction (VR)[VR = 1 − (Σ(synthetics − data)^2/Σ(data)^2)] from the preferred model. All the variance reductions in this study are not distance weighted. To test the contribution of individual seismic stations to the preferred model, we excluded these stations and reran the inversions to document the change in the slip models and waveform fits. Generally, this procedure showed that the slip models look similar to the preferred models. The unweighted variance reduction usually changed by <10% if we excluded one station 30 km or farther from hypocenter. Excluding one near-source station can increase or decrease the unweighted variance reduction by 15%. For each event we did more than 1000 tests, each taking 10–20 min on a typical SUN workstation. We then assigned confidence levels for the preferred slip model on the basis of waveform fits and by comparing the results with aftershock seismicity. While these sensitivity tests only covered a small portion of the total parameter space, this study represents the most thorough attempt to document such uncertainties in finite source inversions. All preferred slip models derived from this study are available in the auxiliary material.[1]

5. Finite Fault Inversion

5.1. Event 1 (09201757)

[20] We have low confidence in the preferred model (Figure 2) for event 1 (Table 1), which occurred 10 min after the main shock when many other aftershocks were occurring. An M_L = 4.61 event occurred 23 km away and 1 s before this event, thereby complicating the preliminary estimation of hypocentral parameters (G. Chang, personal communication, 2002) and the waveforms and thus the finite fault inversion. Sensitivity tests show that the 12 km by 4 km rupture patch is located near 121.04°E, 23.97°N. Its depths range from 6 to 8 km, shallower than the proposed decollement. Our slip model has a maximum slip of 46 cm, while the static stress drop is 5.3 MPa. The variance reduction (VR) of the derived preferred model determined using data from 13 three-component stations is 46%, slightly less than the VR of 48% for the east dipping conjugate fault. We favor the west dipping fault plane because it correlates well with the locations of the aftershocks (Figure 2). To identify preferred station configurations that will help determine the causative fault plane, we forward predicted ground motions using both conjugate fault slip models and found that both models can fit most of the near-source stations relatively well, partly because only three near-source stations were used in the inversion to
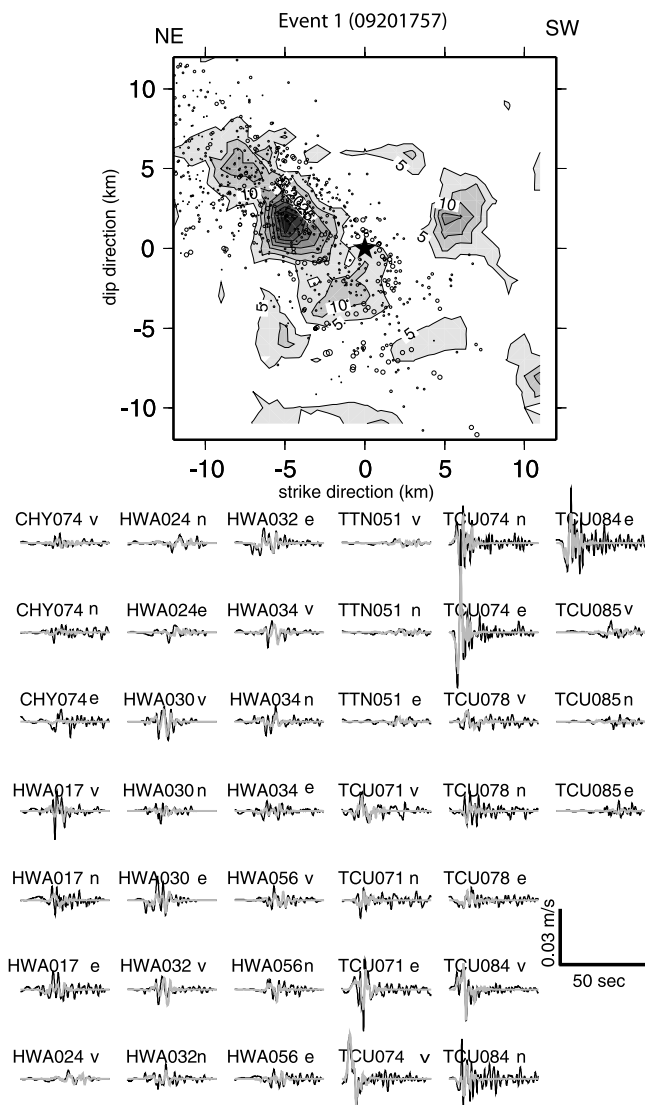

Figure 2. (top) Slip model for event 1 (09201757) and its waveform fits. The star shows the location of the hypocenter which corresponds to a depth of 8 km, and the open circles are the aftershock seismicity within 5 km of the fault, based on data from the Central Weather Bureau and *Kao and Chen* [2000]. We picked the west dipping fault as the preferred model because in addition to the good waveform fits, its slip patch correlates with aftershock seismicity. See Table 1 for parameters and results of this model. (bottom) Filtered velocity waveforms (thick black lines) and the synthetics (thin gray lines).

constrain the models. However, the two conjugate slip models produced very different synthetics east of the hypocenter in the mountainous regions where strong motion data are not currently available. Thus good station coverage in the mountainous region above the decollement will be important for future finite source studies.

[21] Using a 10% decrease in VR as the error threshold, we found that a location error of <4 km still gave a good fit to the waveforms (Figure 1b). Within 20° of error in the focal mechanism, as inferred from change in *P* axis direc-

tion, is acceptable, as shown in Figure 3. Possible focal depths range from 6 to 13 km, and rupture velocities range from 1.3 to 2.6 km/s (Figure 4). Waveform fits are not very sensitive to dislocation risetime. Table 1 lists details of the source parameters and slip models of each of the events.

5.2. Event 2 (09201803)

[22] We assign a high level of confidence to the preferred model (Figure 5) for event 2 (Table 1). The preferred model is strongly controlled by station TCU079 because the VR of the inversion drops to 50% after removing this station from the optimal station configuration. The slip model with TCU079 removed still looks similar to the preferred slip model, and the predicted waveform for TCU079 is good; however, the amplitude is reduced twofold in north and vertical components. Some secondary phases, recorded 20 s after the origin time (i.e., at stations TCU078, TCU079, TCU089), could not be modeled in our inversions, and these late arrivals do not contribute to the preferred slip model. The 10 km by 10 km slip patch is located near 120.82°E and 23.79°N at a depth of 6−8 km. This aftershock ruptured along the southern end of main shock asperity along the Puli-Chusan lineation proposed by *Chi et al.* [2001]. In the cross section view our slip model coincides with the shallowly east dipping fault imaged by a recent reflection profile from *Wang et al.* [2002]. Because the dip angle is very shallow, we suspect that there may be trade-offs between strike and rake. For example, a slip model with a strike and rake of 350° and 80° will be similar to that of 20° and 110° because both the slip direction at each subfault and the location of the subfaults are nearly the same. In the preferred model the low slip near the hypocenter (Figure 5) may be an artifact resulting from an incorrect origin time. However, we tested this by adding a delay of <1 s to the reported origin time. While the slip became more concentrated near the hypocenter, the waveform fits were degraded. To be consistent with other events in this study, we continued to use the reported origin time. Sensitivity tests of focal depth, rupture velocity, and dislocation risetime have patterns similar to that of event 1.

5.3. Event 3 (09202146)

[23] We assign a high level of confidence to the preferred model for event 3 (Figure 1b and Table 1). Unlike the other thrust-type aftershocks, this strike-slip event has N-S oriented horizontal peak ground velocity direction in the coastal plain, perpendicular to the back azimuth direction and consistent with a strike-slip radiation pattern for the *S* wave. The 5 km by 25 km slip patch on a vertical plane mainly ruptured in sedimentary units at depths similar to that of the event 2 slip patch. The maximum slip is 85 cm (Figure 6), and the static stress drop is 3.8 MPa, the lowest among the aftershocks we studied. Location tests show that hypocenters within an elongated region along the strike of the fault gave good waveform fits (Figure 1b). The preferred rake is similar to the dip of the decollement to the north, consistent with the kinematics north of this strike-slip fault. A depth of 18 km places the hypocenter in the basement.

[24] To study whether the dislocation risetime and rupture velocity vary from basement to the overlying sediments, we also inverted this event using four 0.7-s time windows, each
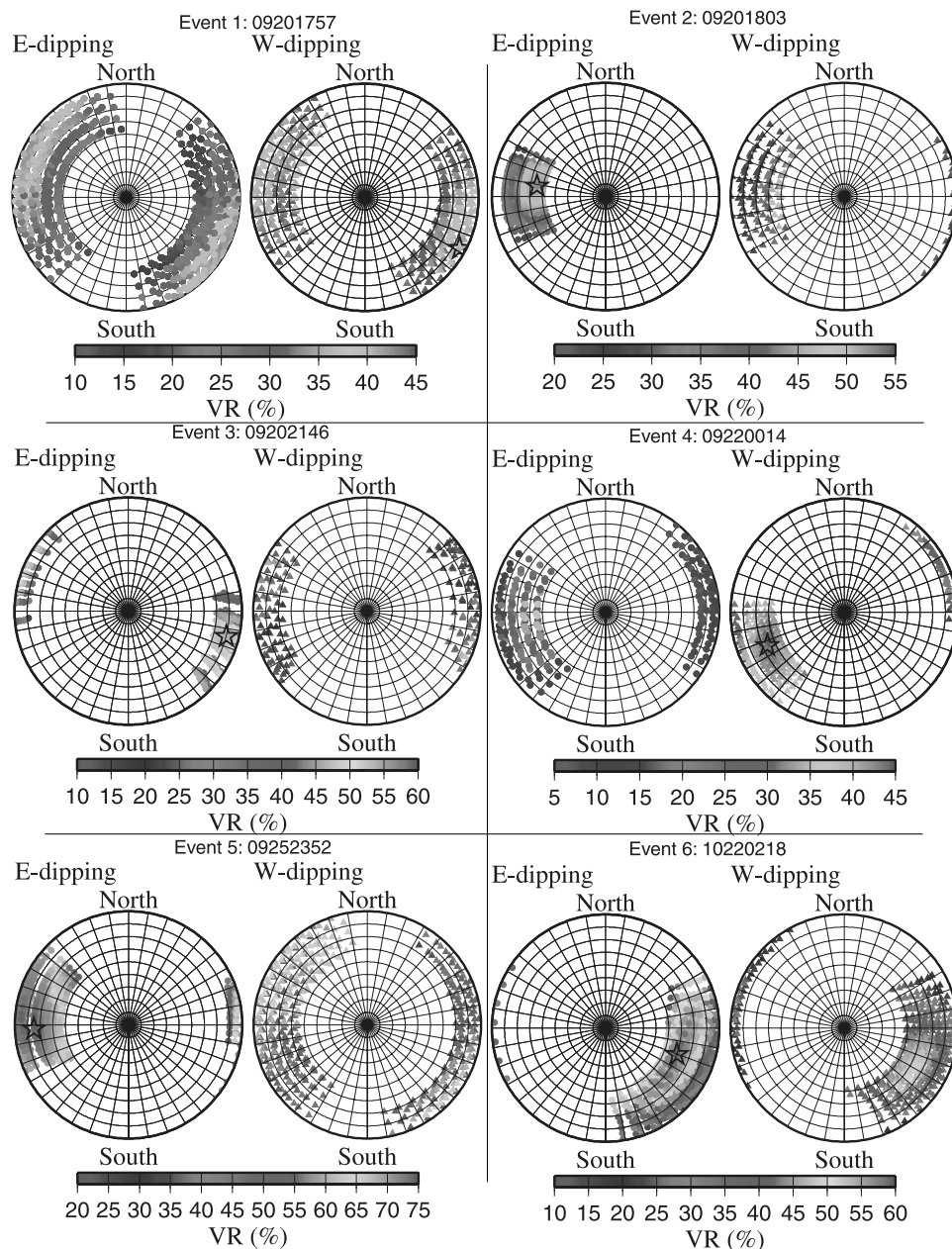
Figure 3. Sensitivity tests on the focal mechanism for each event. The *P* axis of each focal mechanism tested is plotted in lower hemisphere stereonet projection. The left stereonets show the east dipping fault planes, and the right ones show the west dipping planes. Color shows the variance reduction. Note VR deteriorates fastest when the plunge of the *P* axis changes, implying that the waveform fits are most sensitive to the dip, and possibly rake, of the focal mechanism for the thrust events. For the strike-slip aftershock (event 3), VR is more sensitive to strike. The star shows the *P* axis of the preferred focal mechanism. See color version of this figure at back of this issue.

delayed by 0.35 s. We tested six inversions using rupture velocities between 2.0 and 3.0 km/s with 0.2 km/s increment. Rupture velocity between 2.4 and 2.8 km/s gave VR ranging from 56% to 62%. We found a slightly longer (between 0.7 and 1.05 s) dislocation risetime in the sediments, and slip in the sedimentary layers started to transfer to a second time window if the rupture velocity in the inversion is >2.5 km/s. However, the VR only increased 3–6% even though the number of free parameters increased threefold. *F* test results show that the VR increase is not

statistically significant. Thus our preferred model has a single time window.

[25] To test whether this event occurred in the basement, we have studied the relationship between waveform fits and the hypocentral depth assigned in the inversions in more details. For this event the variance reduction decreased 10% when we used a hypocentral depth of shallower than 10 km (Figure 4). Also, the inversions with shallow hypocenters could not generate the large-amplitude particle motion observed at stations CHY080 and CHY035. Our slip model
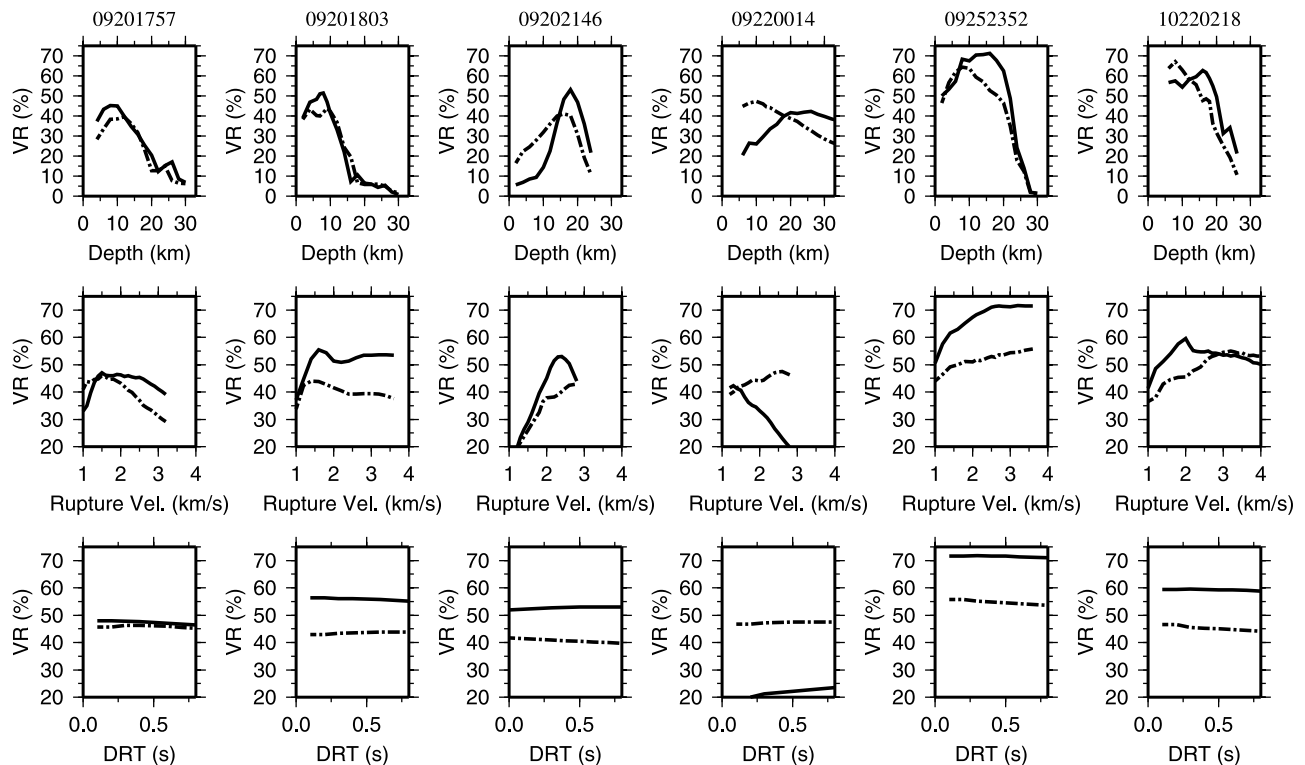
Figure 4. Variation in the waveform fit derived from sensitivity tests of focal depth, rupture velocity, and dislocation risetime (DRT). The solid lines show the east dipping faults, and the dashed lines are the conjugate west dipping faults. For event 3 the solid lines are the NW-SE trending faults. Note that VR drops off quickly if the focal depth varies more than 5 km from the preferred focal depth. VR is also sensitive to the rupture velocity but less sensitive to dislocation risetime. The lack of sensitivity with respect to dislocation risetime is due to the band-limited nature of the inversion.

is strongly controlled by station CHY080. When it is omitted from the inversion, the unweighted VR actually decreases by 12%, even though the VR usually increases when a portion of inverted data is removed. The amount of slip in the basement depends slightly on the level of smoothing and on moment minimization constraints, but the overall ''belt-shaped'' slip patterns in the basement are similar. Actually, near-source unfiltered waveforms show several seconds of small pulses before the major S wave energy arrived, consistent with a slip model with a deep nucleation and a cascade of shallow slip patches. The fault slip is near two of Taiwan's highest mountains, and the waveforms could be complicated because of scattering of the wave field from the rough topography. This event occurred on a fault not previously mapped. However, this northwest trending striking fault is parallel to and located between two other faults shown on the geologic map [*Central Geological Survey*, 2000], which, like this slip model, are bounded at both ends by two NE-SW trending faults.

5.4. Event 4 (09220014)

[26] We assigned a low confidence level to the preferred model for event 4 (Figure 1b and Table 1). Station configuration tests show that the slip model is not dominated by any one station. In contrast to most of the other aftershocks, some stations on the east coast of Taiwan recorded amplitudes larger than those of western stations

at similar epicentral distances. A wide range of focal mechanisms has been reported for this event (Table 1), and reported epicentral depths range from 12.4 to 29 km (*Chen et al.* [2002], Earthquake Research Institute Web site http://www.eri.u-tokyo.ac.jp/~http/AUTO_CMT/auto_cmt.html, Harvard centroid moment tensor, and *Kao and Angelier* [2001]). Sensitivity tests show that the 6 km by 20 km slip patch is located near 121.04°E, 23.85°N with depths ranging from 13 to 24 km. This aftershock ruptured downdip into the basement. Our slip model has a maximum slip of 83 cm (Figure 7) and a static stress drop of 4.6 MPa. It was difficult to interpret which of the conjugate fault planes ruptured because of the uncertainty in the focal depth of this event. The preferred models for both of the conjugate faults give VRs greater than 40%. However, they favor different focal depths and rupture velocities (Figure 4). If the focus is deep and the rupture velocity very slow, it is possible to fit the waveforms well with the east dipping fault. However, seismicity correlates better with the steep west dipping fault, not the east dipping fault above the decollement. Our result is more consistent with the west dipping seismicity below the decollement observed by *Carena et al.* [2002] and *Chen et al.* [2002]. The strike of this slip model shows 30° difference from that of seismicity from *Carena et al.* [2002] but is consistent with the focal mechanism of *Chen et al.* [2002]. This event ruptured along the southern extension of the Sanyi-Puli lineation, and its strike is similar to that of the event 3 to the
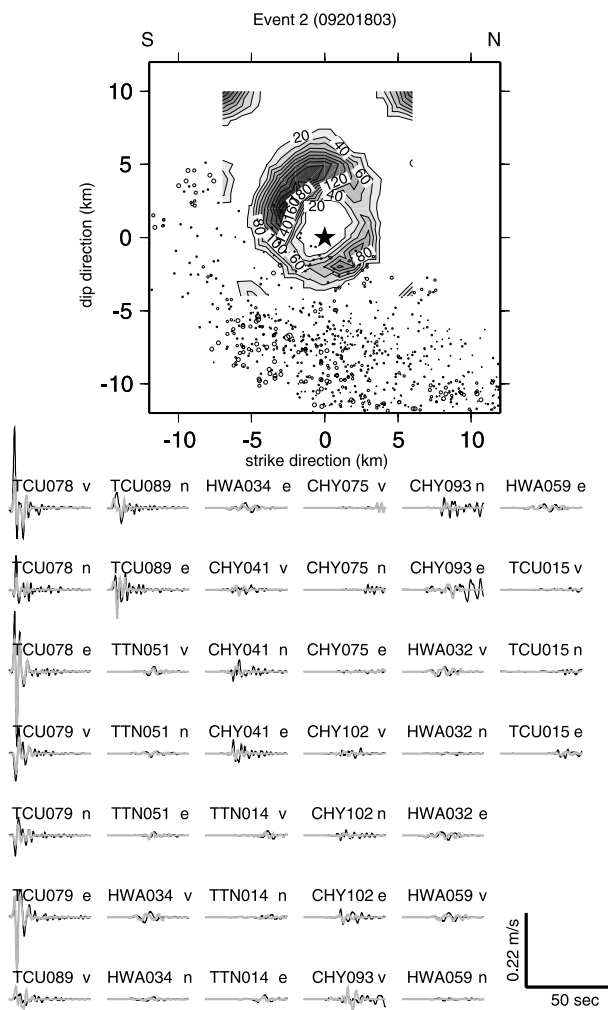
Figure 5. Slip model and waveform fits for event 2 (09201803). The aftershocks are located SW of this east dipping asperity. The east components of stations TCU078 and TCU079 show strong directivity effects.

south, and both events appear to have ruptured in the basement.

5.5. Event 5 (09252352)

[27] We have high confidence in the preferred solution for event 5 (Figure 1b and Table 1) because the VR from the inversion of data from 11 three-component stations is 72% (Figure 8). The slip model is strongly controlled by station TCU078. *Chi and Dreger* [2002] published preliminary finite fault inversion results for this event. Here, we have performed additional sensitivity tests and included them for completeness. Waveforms recorded southwest of the epicenter had large amplitudes. The 6 km by 22 km slip patch is near 121.00°E, 23.81°N with depths from 12 to 18 km. Our slip model has a 162 cm maximum slip and a static stress drop of 5.9 MPa (Figure 8). In map view and in cross section this event appears to be a downdip extension of event 2, although the dips of the two events are slightly different. Because of the uncertainty in depth and the steeper dip angle, this event may have been on a step down of the decollement

or a splay fault above it. Both events ruptured along the Puli-Chusan lineation and are sandwiched between aftershock seismicity to the south and main shock rupture to the north.

5.6. Event 6 (10220218)

[28] Event 6 (Figure 1b and Table 1) caused at least 12 buildings to collapse near the city of Chai-Yi. Because fits from both conjugate faults were equally good, we assigned a low level of confidence to the preferred model for this event. More than 30 strong motion stations at epicentral distance less than 25 km recorded this event and at all azimuths.

[29] The near-source waveforms may have been complicated by the 3-D basin structures, which may explain the
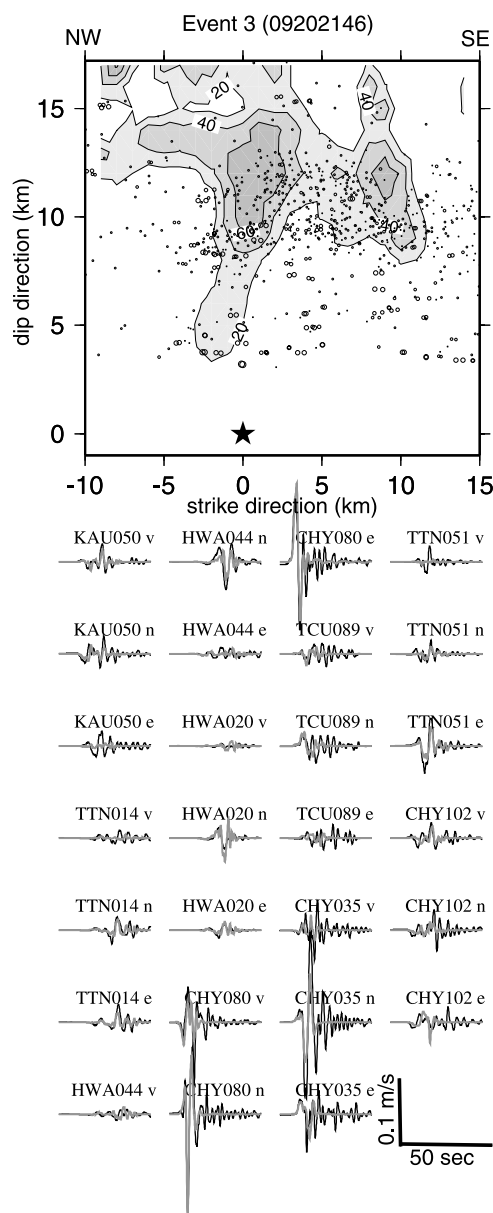

Figure 6. Slip model and waveform fits for event 3 (09202146). The focal depth for this event is 18 km, but the asperity mainly ruptures at shallow depth in sedimentary layers. This event shows strong evidence of active basement deformation affecting the shallow crust structures.
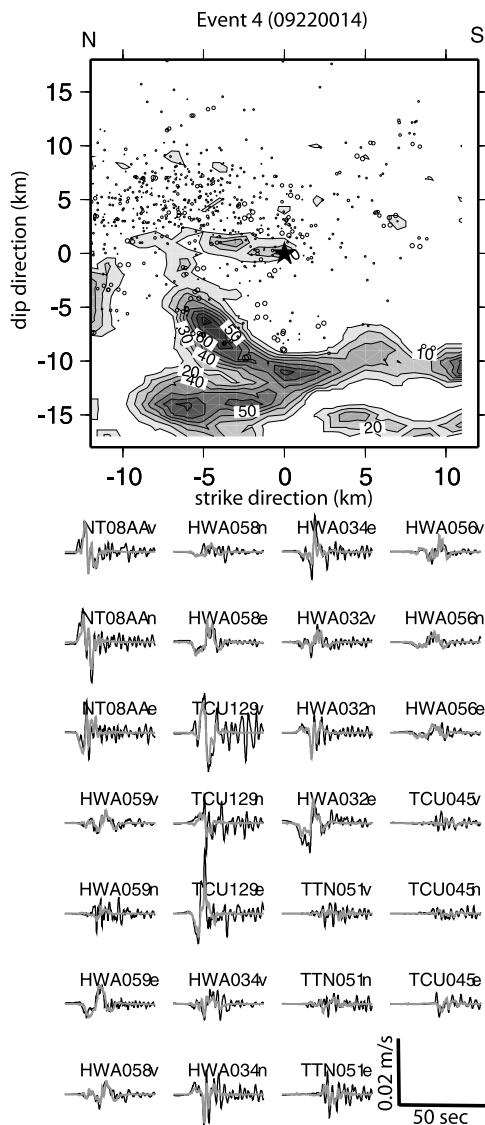
Figure 7. Slip model and waveform fits for event 4 (09220014). The aftershocks seem to surround the shallow part of the asperity. Many stations east of the epicenter (e.g., all the HWA stations) show surprisingly large amplitudes compared with the western stations, possibly due to a directivity effect from this west dipping basement fault.

wide range of moment tensor solutions and differences of up to 5 s in origin time reported by different agencies (Table 1). In a preliminary finite fault inversion using data from six strong motion stations, the west dipping fault produced a higher variance reduction. By adding eight additional stations in the course of station configuration tests, we found that the variance reduction of the west dipping plane is slightly higher if the focal depth is ~8 km. However, the east dipping plane also produced good waveform fits if we used a focal depth of 16 km (Figure 9). We tentatively picked the east dipping fault plane as the preferred model only because most of the focal depths reported for this event are consistently around 16 km and regional geologic interpretation favors east dipping faults. On the other hand, unpublished hypoDD relocations of the seismicity in this

region became available (C.-H. Chan, personal communication, 2003) while we revised this manuscript, and they are more consistent with the west dipping slip model. Because of the difficulty of determining the causative fault plane for this event, we have included both the east and west dipping slip models in our auxiliary material[1].

6. Sensitivity of the Inversions to the Station Used and to Changes in the Source Parameters

[30] Because more than 200 stations recorded each aftershock, the most challenging part of this study was to find the configuration of stations which gave good azimuthal
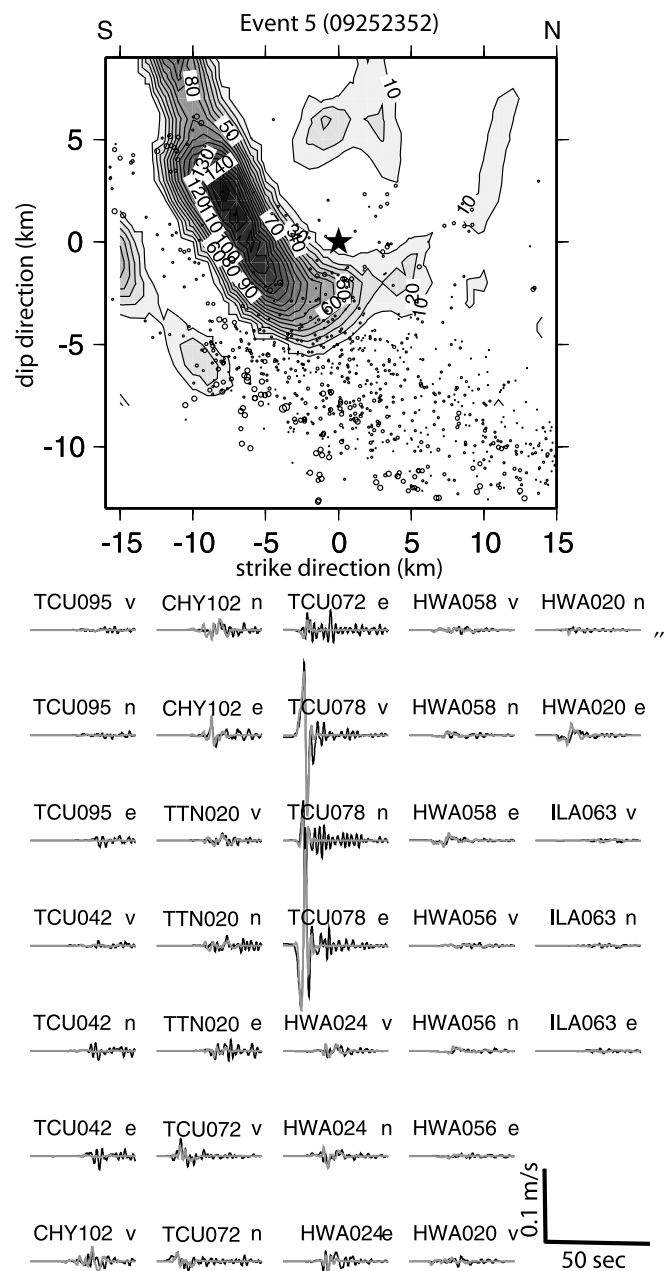

Figure 8. Slip model and waveform fits for event 5 (09252352). The aftershocks are located south of the slip patch. Chi-Chi main shock rupture stopped north of this slip patch.
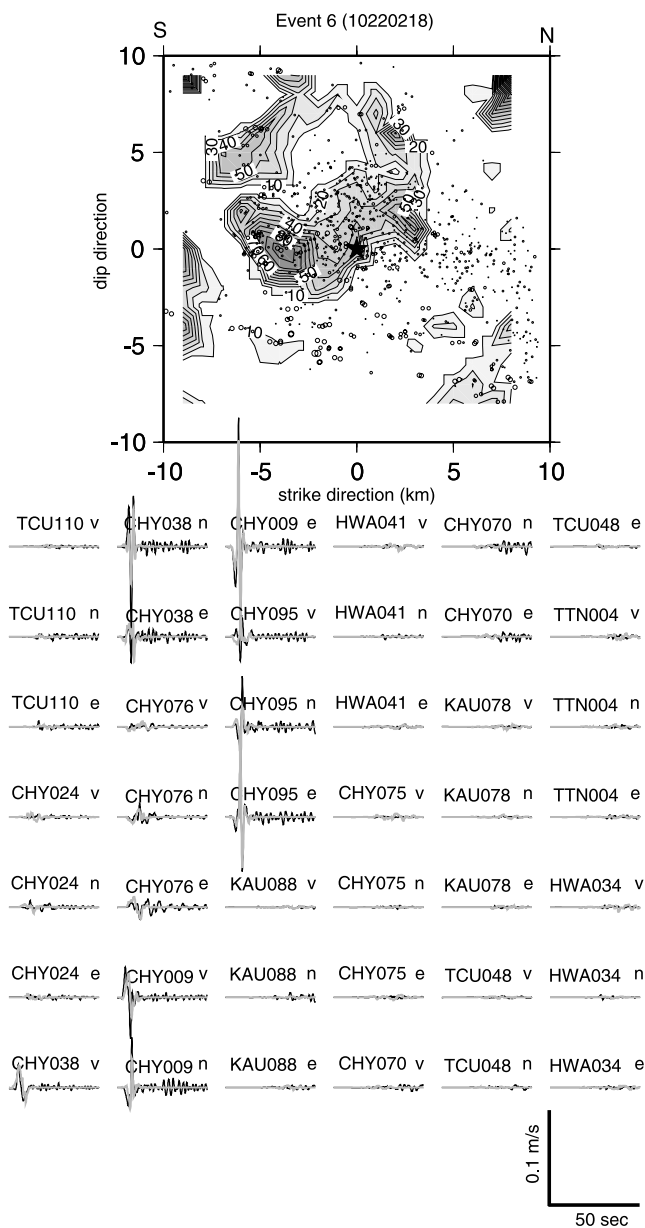
Figure 9. Slip model and waveform fits for event 6 (10220218). Even though the waveform fits from 14 stations are very good, we assigned a low confidence level for this model because we could not determine the causative fault plane conclusively. The aftershock seismicity is also scattered and hard to interpret.

coverage and enough waveforms with paths that could be represented by the simple 1-D crustal model that we used to calculate the Green's functions. Many of the strong motion stations may have timing problems [*Lee et al.*, 2001] and may be affected by the 3-D heterogeneity of velocity structures along the path. If we randomly selected 20–40 stations with good azimuthal coverage and inverted them, the resulting scalar moments were small and the variance reduction low. For this particular study, we chose to use between 9 and 14 stations. We picked the stations by trial and error and by eliminating stations with abnormal waveforms compared to neighboring stations. In particular,

we chose stations on the basis of their performance in initial inversions using preliminary source parameters derived from those reported by various agencies; thus the selection of stations may be biased if the reported source parameters are incorrect. To make our analysis more robust, we made a concerted effort to test any newly reported source parameters as they became available.

[31] The focal mechanism is one of the most important source parameters in our inversion. We did a grid search on the focal mechanism parameters and found that overall the waveform fits are strongly controlled by the dip angle for the thrust events. A deviation of $20°$ from preferred P axis direction will decrease the VR by 10% (Figure 3); for example, VR will decrease from 50% to 40%. However, the single strike-slip event among these after-shocks is more sensitive to strike and rake than the thrust events. This may be related to the maximum amplitude of the shear wave radiation patterns. The large-amplitude waveforms are located updip of the thrust and along strike of a strike-slip fault and are sensitive to the dip of the thrust or the strike of the strike-slip fault. For strike-slip faults this poses only a small problem because their causative faults and strikes can usually be identified easily by aftershock distributions with more accurate epicentral locations than focal depths. However, for blind thrusts it is possible that discrepancies in focal depth are >5 km and in the dip of preliminary focal mechanisms may be up to $20°$. This could cause problems for routine finite source inversions that rely on an a priori knowledge of the fault orientation.

[32] Good hypocentral information is also very important. We found that the epicentral location has a large influence on the waveform fits (Figure 1b). When we shifted the hypocenter by 5 km from the optimal hypocenter, the VR of the synthetics decreased about 10%. Because of the average 5 km station spacing of the seismic network the initial reported epicentral locations for these aftershocks are usually pretty accurate already. Except for event 4, we also found that an error of 5 km in focal depth will reduce the VR by 10%. For comparison, the asperities that we derived from this study have dimensions ranging from 5 km by 10 km to 6 km by 22 km. So the error bounds are roughly similar to the small dimension of the slip distribution.

[33] Compared to the tests of focal mechanisms and hypocentral locations, we found that the inversions in this study are not very sensitive to changes in the dislocation risetime. This is, in part, due to the relatively small size of the events and the low-pass filter corner applied to the data and Green's functions. Empirical relationships indicate that the average risetimes for such events should be short, at or below limit of resolution of our tests.

7. Implications for Regional Tectonics

[34] We have proposed that only two of the aftershocks discussed here occurred in the vicinity of the proposed east dipping decollement. One west dipping back thrust event ruptured above the decollement; one strike-slip aftershock nucleated in the basement then ruptured through the over-lying sedimentary layers; and two aftershocks occurred on basement-involved reverse faults (Figure 1b).
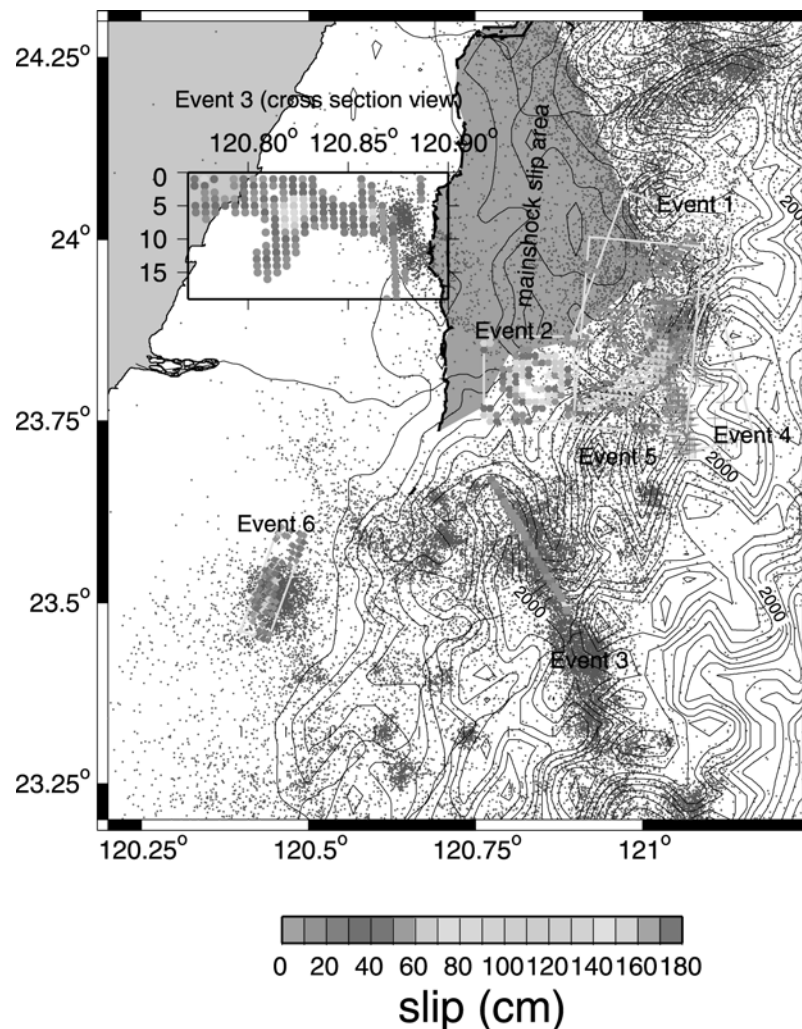
Figure 10. Slip models from this study are plotted on the black topographic contour map. The dark gray dots are the aftershock seismicity from *Kao and Chen* [2000] and the Central Weather Bureau. Note that event 5 ruptured just east of event 2. Event 3 ruptured along NW trend in the aftershock seismicity. The cross section view of the slip model for event 3 is plotted in the inset. See color version of this figure at back of this issue.

[35] The two aftershocks in the vicinity of the decollement ruptured along the Puli-Chusan lineation. In cross section these two aftershocks form a flat ramp geometry. However, given the uncertainty in depth, event 4 could have been at a shallower depth, becoming a splay fault branching up from the decollement.

[36] The west dipping back thrust slip model above the decollement from event 1, along with the east dipping decollement that ruptured during the main shock, forms a pop-up structure that was proposed to explain the pure shear type of microstructure deformation observed in the mountains to the north [*Clark et al.*, 1993]. Sandbox modeling by *Lu et al.* [2002] also predicted back thrusting in this region.

[37] Two of the aftershocks show basement-involved reverse faulting. Although both of them were assigned low confidence levels, the deep focal depths determined from our analysis are robust, as inversions using shallow focal depths could not generate satisfactory waveform fits. The steep dip angles of our preferred fault models suggest that these events ruptured on preexisting weak zones, presumably normal/strike-slip faults along the passive margin. In fact, many studies have proposed reactivated normal faults in the basement inferred from oil company reflection data and well log data [e.g., *Suppe*, 1984]. Our results suggest that such structures may currently be seismogenic. As a result, not all the active deformations are above the decollement.

[38] Event 4 ruptured on a west dipping fault under the decollement, which is consistent with the results from *Carena et al.* [2002] and *Chen et al.* [2002]. Repeated west dipping reverse faulting events under the decollement could uplift the western part of the decollement over geologic time. Thus, if the regional decollement is flat in this region [*Carena et al.*, 2002] or only dips slightly to the south [*Wang et al.*, 2002], this type of basement reverse faulting could be a transient or young feature. Another possibility is a duplex style of deformation between two subhorizontal main detachment faults.

[39] Event 6 occurred on a basement-involved reverse fault under the western plains. Although at greater depth, base-
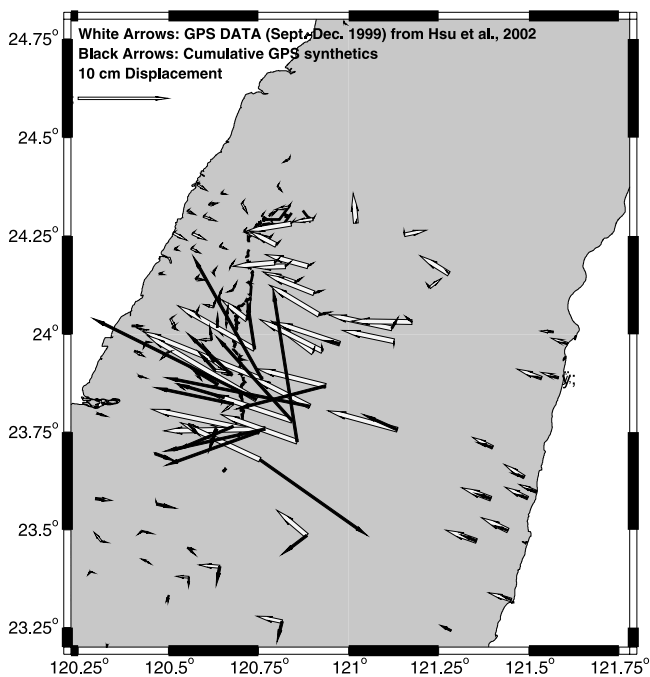
Figure 11. Postseismic GPS displacement [*Hsu et al.*, 2002] as large light shaded arrows. Cumulative synthetic GPS displacements derived from the six aftershock slip models using *Okada*'s [1992] method are shown as small black arrows. The estimate aftershock deformation is of the same order as the postseismic deformation, and the pattern in magnitude is similar. Deviations in the vectors may indicate other postseismic processes and/or the deformation due to other large unmodeled aftershocks. One station near 120.76°E and 23.7°N shows flipped forward predicted GPS displacements. This station is near the nodal plane of the strike-slip aftershock (event 3) so the discrepancy may be due to slight errors in its hypocenter and/or the strike of the fault or due to nonplanar fault rupture.

ment faults in this region can pose significant seismic hazard because they lie directly beneath cities. The strike of this fault is subparallel to the topographic lineation farther to the east (Figure 10). Like other basement-involved aftershocks in this study, this aftershock's fault plane may be controlled by the structures in the underthrusting passive margin.

[40] Event 3 is a strike-slip event initiated within the basement, but the asperity is mostly concentrated at shallow depth along and just above the proposed decollement. In fact, the slip seems to have a rake consistent with the shallow dip of the decollement 5–10 km to the north. Our result provides evidence of basement deformation propagating to the overlying sedimentary layers and generating large slip at shallow depth. If true, this will be one of the first studies that show deformation style above the decollement being influenced by active deformation within the basement. Because of the shallow asperity we predicted that deformation may be detectable in GPS measurements.

[41] Except for event 4, the azimuths of the *P* axes derived from our preferred models are roughly about N70°E (Figure 3), consistent with the current relative plate motion. However, the fault plane orientations of these six aftershocks are very different. This suggests that the kinematics of these

large aftershocks is mainly controlled by tectonic stress, although they occurred on preexisting weak zones that do not have similar attitudes. The triggering of the aftershocks may be closely related to stress perturbation due to the main shock rupture, suggested by the static stress transfer study of the main shock [*Wang and Chen*, 2001] and by *Kao and Angelier* [2001] on the basis of moment tensor data.

[42] Postseismic deformation has been studied extensively for recent large earthquakes [e.g., *Bürgmann et al.*, 2002]. There is an excellent postseismic GPS data set [*Hsu et al.*, 2002] for the Chi-Chi earthquake sequence. *Chi and Dreger* [2002] argued for large GPS signals from event 5 contributing to the observed postseismic deformation, composing up to 30% of the total postseismic displacement at several stations near this event. Here we forward predicted the GPS deformation using a half-space elastic structure [*Okada*, 1992] for the slip models of the six aftershocks. The cumulative aftershock-related displacement from these six aftershocks was as high as 10 cm at some GPS stations, explaining at least 80% of the postseismic deformation observed in the southern half of the hanging block where these aftershocks occurred (Figure 11).

[43] The fact that the observed and estimated postseismic deformation vectors differ indicates that processes other than these large aftershocks are also occurring. This could include viscoelastic postseismic deformation mechanisms as well as the other large unmodeled aftershocks. Besides these six events, there were at least three other *M* > 6 aftershocks that remain to be studied and should be investigated to allow improved resolution of nonseismic postseismic deformation.

8. Conclusion

[44] We have inverted strong motion data to determine the finite source parameters for six large aftershocks (five dip slip and one strike slip) of the 1999 Chi-Chi, Taiwan, earthquake sequence (Figure 10). We tested more than 1000 inversions for each event and documented the variation in the waveform fit due to different input parameters, including changes in the station configuration, the focal mechanism, the hypocentral location, the rupture velocity, and the dislocation risetime. We then assigned confidence levels for each event on the basis of these tests and by comparing the resulting slip models with seismicity.

[45] Three of the aftershock slip models were assigned high levels of confidence due to good waveform fits and good correlation with results from reflection data, seismicity, and geologic maps. Particularly, the slip model for event 2 correctly depicted the fault orientation imaged by recently released reflection data.

[46] Except for one strike-slip event, which started deep, and one event located to the west in the footwall of the main shock, the ruptures of the other events began in the vicinity of the decollement near the main shock slip. We have high confidence in the slip models that ruptured updip to the west on the decollement. However, there is also strong evidence of updip rupture to the east, forming a pop-up structure, or downdip rupture to the west below the decollement, suggesting some aftershocks did not rupture on the decollement but on structures that root into the decollement.

[47] We use the sensitivity test results to place bounds on the source parameter space. In another words, we have

tested different input parameters to determine their influence on inversion results. For these M_w 5.8–6.4 earthquakes in Taiwan region we found that inversions using 10 stations usually gave stable results, provided there are no timing errors. Jackknife tests show that with fewer stations we can still derive similar slip models, but the results are not as robust. Using accurate focal mechanisms dramatically improves the waveform fits and the slip model. Particularly for the thrust events, the input dip angle must be correct to within 20° for the events we studied. For the single strike-slip event the strike must also be within 20° of the true strike. Hypocentral locations must be within 5 km of the actual locations, which is close to the smaller dimension of the slip patches that we modeled. The inversions were not very sensitive to the dislocation risetime due to the band-limited nature of the analysis. Although these may not be general results, this study shows that significant trade-offs between the fixed parameters of the inversion can introduce significant bias in the results.

[48] We documented the spatial resolution of large after-shock slip and their P axis directions. Two aftershocks ruptured along the Puli-Chusan lineation, where the main shock rupture stopped. Three aftershocks show evidence of basement-involved deformation. In particular, we found a strike-slip event that nucleated within the basement, but the asperity is mainly located within the overlying sediments, strongly suggesting that basement structures play an important role in surface deformation. Five out of the six slip models have P axes with azimuths consistent with current relative plate motion. However, the fault orientations of these aftershocks are very different. We interpreted this as large aftershocks being triggered by the stress perturbation of the main shock on preexisting structures. However, the kinematics of the aftershocks remains consistent with regional tectonic stress.

References

Aki, K., and P. G. Richards (1980), *Quantitative Seismology*, W. H. Freeman, New York.

Bürgmann, R., S. Ergintav, P. Segall, E. H. Hearn, S. C. McClusky, R. E. Reilinger, H. Woith, and J. Zschau (2002), Time-dependent distributed afterslip on and deep below the Izmit earthquake rupture, *Bull. Seismol. Soc. Am.*, 92, 126–137.

Carena, S., J. Suppe, and H. Kao (2002), Active detachment of Taiwan illuminated by small earthquakes and its control of first-order topography, *Geology*, 30(10), 935–938.

Central Geological Survey (2000), Geologic map of Taiwan, scale 1:500,000, Minist. of Econ. Affairs of Taiwan, Taipei.

Chen, K.-C., B.-S. Huang, J.-H. Wang, and H.-Y. Yen (2002), Conjugate thrust faulting associated with the 1999 Chi-Chi, Taiwan, earthquake sequence, *Geophys. Res. Lett.*, 29(8), 1277, doi:10.1029/2001GL014250.

Chi, W.-C., and D. Dreger (2002), Finite fault inversion of the September 25, 1999 (M_w = 6.4) Taiwan earthquake: Implications for GPS displace-ments of Chi-Chi, Taiwan earthquake sequence, *Geophys. Res. Lett.*, 29(14), 1694, doi:10.1029/2002GL015237.

Chi, W.-C., D. Dreger, and A. Kaverina (2001), Finite-source modeling of the 1999 Taiwan (Chi-Chi) earthquake derived from a dense strong-motion network, *Bull. Seismol. Soc. Am.*, 91, 1144–1157.

Clark, M. B., D. Fisher, C.-Y. Lu, and C.-H. Chen (1993), Kinematic analyses of the Hsuehshan Range, Taiwan: A large-scale pop-up structure source, *Tectonics*, 12(1), 205–218.

Hartzell, S. H., and T. H. Heaton (1983), Inversion of strong ground motion and teleseismic waveform data for the fault rupture history of the 1979 Imperial Valley, California, earthquake, *Bull. Seismol. Soc. Am.*, 73, 1553–1583.

Hirata, N., S. Sakai, Z.-S. Liaw, Y.-B. Tsai, and S.-B. Yu (2000), Aftershock observations of the 1999 Chi-Chi, Taiwan earthquake, *Bull. Earthquake Res. Inst. Univ. Tokyo*, 75(1), 33–46.

Hsu, Y.-J., N. Bechor, P. Segall, S.-B. Yu, L.-C. Kuo, and K.-F. Ma (2002), Rapid afterslip following the 1999 Chi-Chi, Taiwan earthquake, *Geophys. Res. Lett.*, 29(16), 1754, doi:10.1029/2002GL014967.

Ji, C., D. V. Helmberger, T.-R. A. Song, K.-F. Ma, and D. J. Wald (2001), Slip distribution and tectonic implication of the 1999 Chi-Chi, Taiwan, earthquake, *Geophys. Res. Lett.*, 28(23), 4379–4382.

Johnson, K. M., Y. J. Hsu, P. Segall, and S. B. Yu (2001), Fault geo-metry and slip distribution of the 1999 Chi-Chi, Taiwan earthquake imaged from inversion of GPS data, *Geophys. Res. Lett.*, 28(11), 2285–2288.

Kao, H., and J. Angelier (2001), The Chichi earthquake sequence, Taiwan: Results from source parameter and stress tensor inversions (in French and English), *Sci. Terre Planetes*, 333(1), 65–80.

Kao, H., and W.-P. Chen (2000), The Chi-Chi earthquake sequence: Active, out-of-sequence thrust faulting in Taiwan, *Science*, 288, 2346–2349.

Kikuchi, M., Y. Yagi, and Y. Yamanaka (2000), Source process of the Chi-Chi, Taiwan earthquake of September 21, 1999 inferred from teleseis-mic body waves, *Bull. Earthquake Res. Inst. Univ. Tokyo*, 75(1), 1–13.

Lawson, C., and R. Hanson (1974), *Solving Least Squares Problems*, 337 pp., Prentice-Hall, Englewood Cliffs, N. J.

Lee, W. H. K., T. C. Shin, K. W. Kuo, K. C. Chen, and C.-F. Wu (2001), CWB free-field strong-motion data from the 21 September Chi-Chi, Taiwan, earthquake, *Bull. Seismol. Soc. Am.*, 91, 1370–1376.

Loevenbruck, A., R. Cattin, X. Le Pichon, M.-L. Courty, and S.-B. Yu (2001), Seismic cycle in Taiwan derived from GPS measurements (in French and English), *Sci. Terre Planetes*, 333(1), 57–64.

Lu, C.-Y., H.-T. Chu, J.-C. Lee, Y.-C. Chan, K.-J. Chang, and F. Mouthereau (2002), The 1999 Chi-Chi Taiwan earthquake and basement impact thrust kinematics, *West. Pac. Earth Sci.*, 29(2), 181–190.

Ma, K.-F., T.-R. The, S.-J. Lee, and H.-I. Wu (2000), Spatial slip distribution of the September 20, 1999, Chi-Chi, Taiwan, earthquake (M_w 7. 6); inverted from teleseismic data, *Geophys. Res. Lett.*, 27(20), 3417–3420.

Ma, K.-F., J. Mori, S.-J. Lee, and S.-B. Yu (2001), Spatial and temporal distribution of slip for the 1999 Chi-Chi, Taiwan, earthquake, *Bull. Seis-mol. Soc. Am.*, 91, 1069–1087.

Mori, J., and K.-F. Ma (2000), Slip velocity estimates of the 1999 Chi-Chi, Taiwan earthquake, New observations of fault dynamics, *Eos Trans. AGU*, 81(22), West Pac. Geophys. Meet. Suppl., Abstract S51D-03.

Okada, Y. (1992), Internal deformation due to shear and tensile faults in a half-space, *Bull. Seismol. Soc. Am.*, 82, 1018–1040.

Rau, R.-J., and F. Wu (1995), Tomographic imaging of lithospheric struc-tures under Taiwan, *Earth Planet. Sci. Lett.*, 133, 517–532.

Saikia, C. K. (1994), Modified frequency-wave-number algorithm for regional seismograms using Filon's quadrature-modeling of $L(g)$ waves in eastern North America, *Geophys. J. Int.*, 118, 142–158.

Sommerville, P., K. Irikura, R. Graves, S. Sawada, D. Wald, N. Abrahamson, Y. Iwasaki, T. Kagawa, N. Smith, and A. Kowada (1999), Characterizing crustal earthquake slip models for the prediction of strong ground motion, *Seismol. Res. Lett.*, 70(1), 59–80.

Suppe, J. (1981), Mechanics of mountain-building and metamorphism in Taiwan, *Mem. Geol. Soc. China*, 4, 67–89.

Suppe, J. (1984), Seismic interpretation of the compressively reactivated normal fault near Hsinchu, western Taiwan, *Pet. Geol. Taiwan*, 20, 85–96.

Wang, C.-Y., C.-L. Li, F.-C. Su, M.-T. Leu, M.-S. We, S.-H. Lai, and C.-C. Chern (2002), Structural mapping of the 1999 Chi-Chi earth-quake fault, Taiwan by seismic reflection methods, *TAO*, 13(3), 211–226.

Wang, W.-H., and C.-H. Chen (2001), Static stress transferred by the 1999 Chi-Chi, Taiwan, earthquake: Effects on the stability of the surrounding fault systems and aftershock triggering with a 3D fault-slip model, *Bull. Seismol. Soc. Am.*, 91, 1041–1052.

Wu, C., M. Takeo, and S. Ide (2001), Source process of the Chi-Chi earthquake: A joint inversion of strong motion data and Global Positioning System data with a multifault model, *Bull. Seismol. Soc. Am.*, *91*, 1128–1143.

Yagi, Y., and M. Kikuchi (2000), Source rupture process of the Chi-Chi, Taiwan, earthquake of 1999, obtained by seismic wave and GPS data, *Eos Trans. AGU*, *81*(22), West Pac. Geophys. Meet. Suppl., Abstract S21A-05.

Yu, S.-B., et al. (2001), Preseismic deformation and coseismic displacements associated with the 1999 Chi-Chi, Taiwan, earthquake, *Bull. Seismol. Soc. Am.*, *91*, 995–1012.

Zeng, Y., and C.-H. Chen (2001), Fault rupture process of the 20 September 1999 Chi-Chi, Taiwan, earthquake, *Bull. Seismol. Soc. Am.*, *91*, 1088–1098.

W.-C. Chi, Seismological Laboratory, California Institute of Technology, MC 252-21, 1200 E California Blvd., Pasadena, CA 91125-0001, USA. (wchi@gps.caltech.edu)

D. Dreger, Seismological Laboratory, University of California, 281 McCone Hall, Berkeley, CA 94720, USA. (dreger@seismo.berkeley.edu)
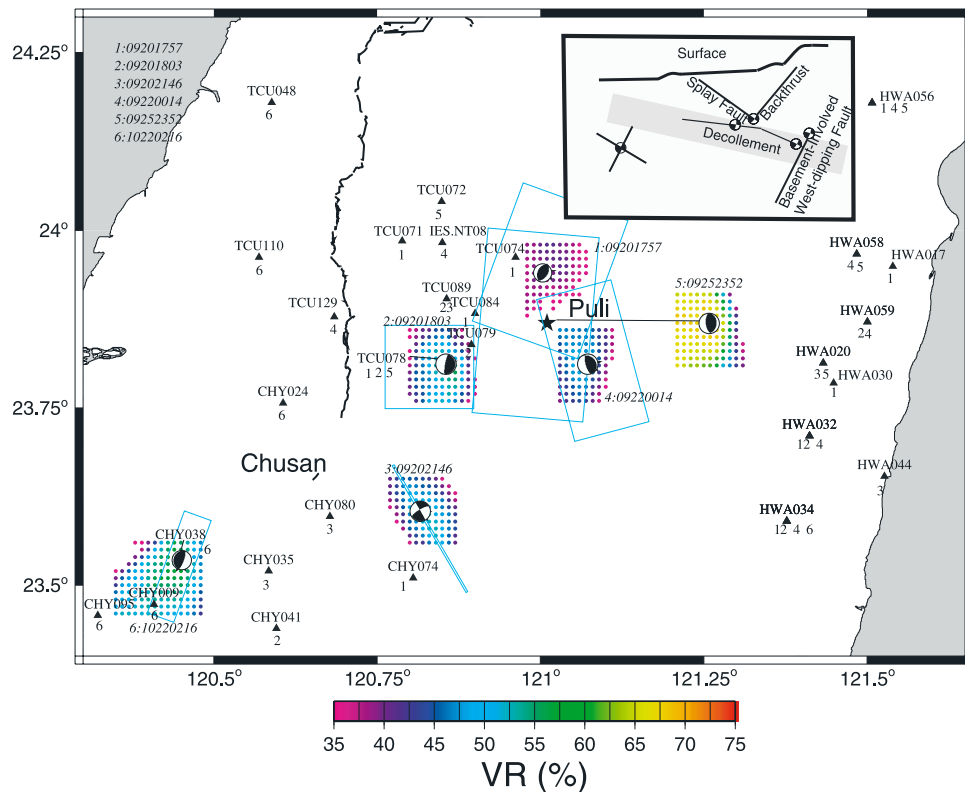
Figure 1b. Enlargement of box on Figure 1a. The focal mechanisms are plotted at the preferred epicenters. The dot color shows the variance reduction derived from inversions using that particular location as epicenter. It shows how rapidly the waveform fits, measured by variance reduction (VR), deteriorate if the epicentral information is incorrect. Results for event 5 are shifted to the east for clear presentation. The blue rectangles are the fault dimensions of the preferred slip models. Note that events 2 and 5 are located along the lineation defined by the towns Puli and Chusan. *Chi et al.* [2001] have proposed that main shock rupture stopped along this lineation. The inset cross section shows a schematic with possible rupture scenarios for the aftershocks that we studied. Depending on the causative fault plane and its dip angle, these aftershocks might have ruptured on the decollement, an east dipping splay fault, a back thrust, or a basement-involved fault.
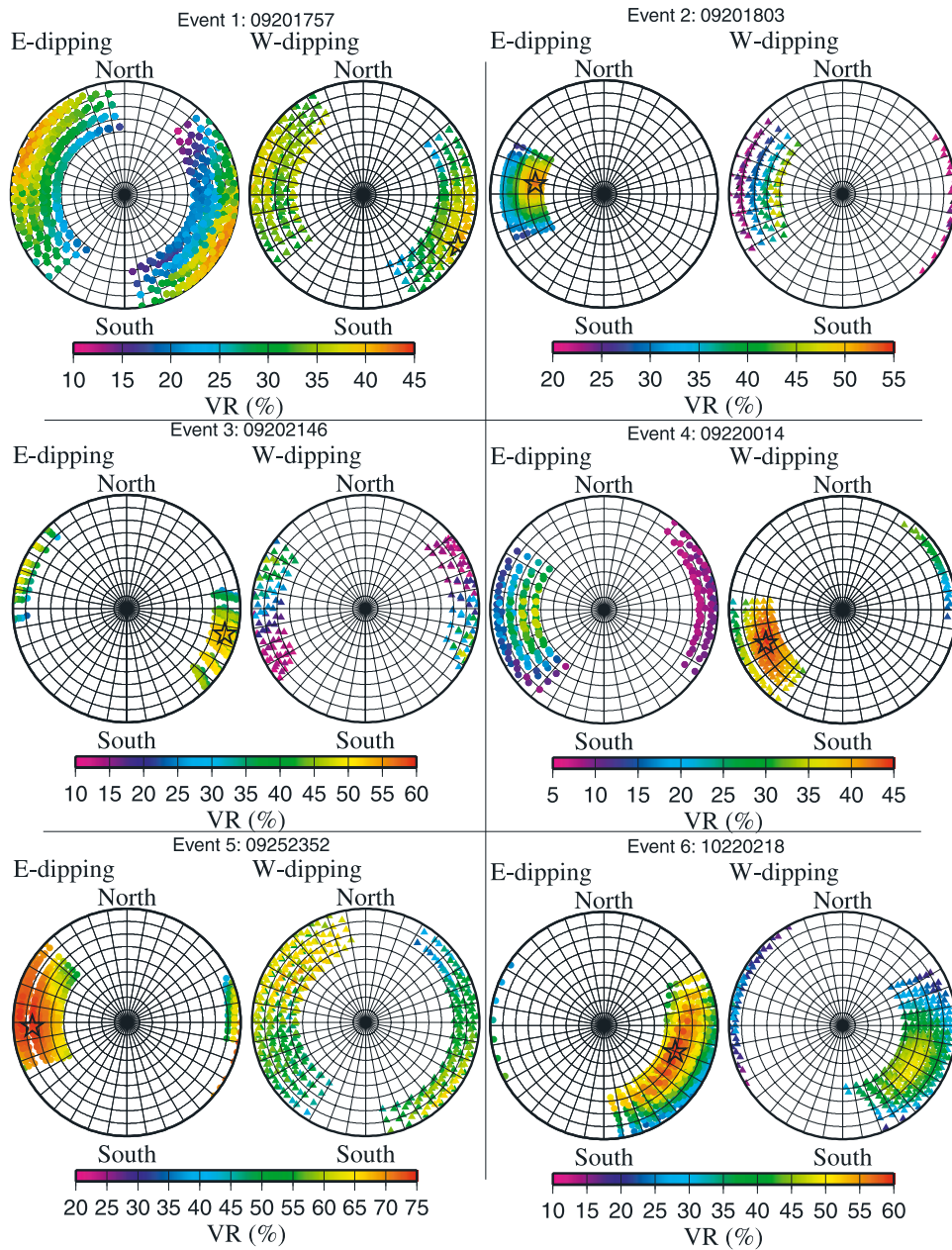
Figure 3. Sensitivity tests on the focal mechanism for each event. The *P* axis of each focal mechanism tested is plotted in lower hemisphere stereonet projection. The left stereonets show the east dipping fault planes, and the right ones show the west dipping planes. Color shows the variance reduction. Note VR deteriorates fastest when the plunge of the *P* axis changes, implying that the waveform fits are most sensitive to the dip, and possibly rake, of the focal mechanism for the thrust events. For the strike-slip aftershock (event 3), VR is more sensitive to strike. The star shows the *P* axis of the preferred focal mechanism.
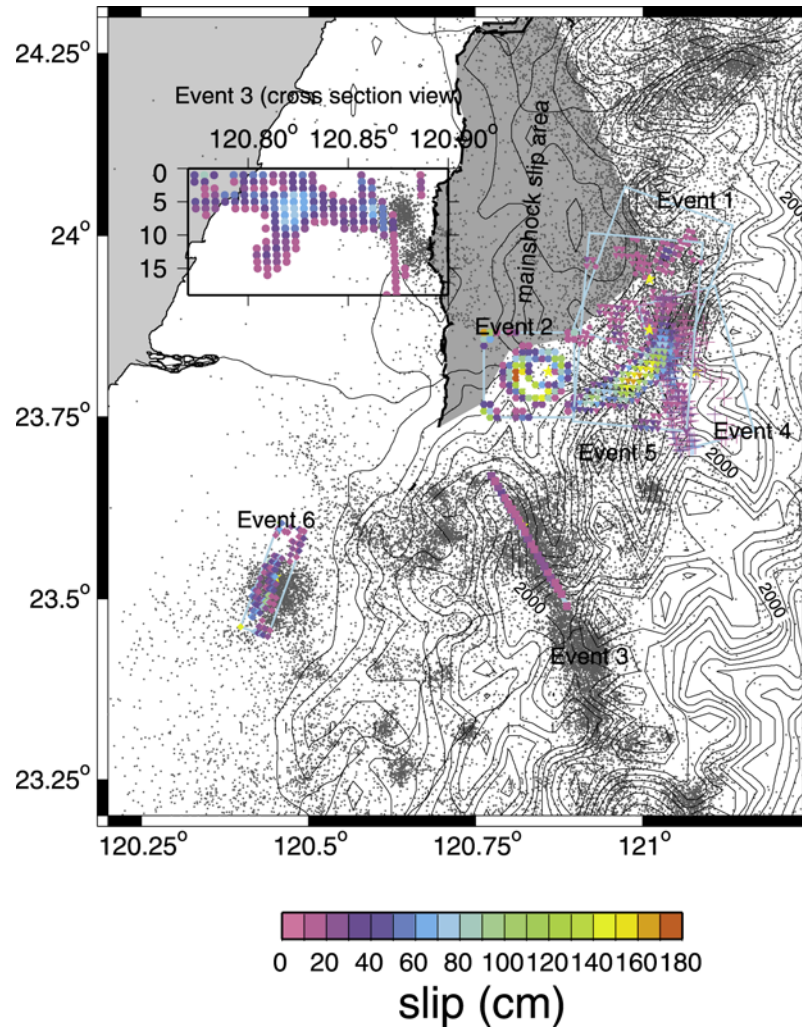
Figure 10. Slip models from this study are plotted on the black topographic contour map. The dark gray dots are the aftershock seismicity from *Kao and Chen* [2000] and the Central Weather Bureau. Note that event 5 ruptured just east of event 2. Event 3 ruptured along NW trend in the aftershock seismicity. The cross section view of the slip model for event 3 is plotted in the inset.